Journal of Alloys and Compounds 898 (2022) 162952

Contents lists available at ScienceDirect

Journal of Alloys and Compounds

journal homepage: www.elsevier.com/locate/jalcom

Prussian blue-graphene oxide composite cathode for a sodium-ion capacitor with improved cyclic stability and energy density

Song Yeul Lee, Joo-Yeon Park, Hyun-Jae Kim, Yun-Sung Lee*, Yong Il Park*

School of Chemical Engineering, Chonnam National University, Gwangju 61186, Republic of Korea

ARTICLE INFO

Article history:
Received 10 July 2021
Received in revised form 15 November 2021
Accepted 23 November 2021
Available online 26 November 2021

Keywords:
Sodium
Capacitor
Energy storage
Battery-type cathode
Hybrid capacitor

ABSTRACT

For applications involving sodium-ion capacitor (SIC) with high energy and high power, it is necessary to develop cathode materials with high operating voltage, high capacity, and excellent cyclic stability. Prussian blue and its analogs are considered promising candidates for cathode materials owing to their high energy and high stability resulting from their open framework structure. We demonstrate that the Prussian blue-graphene oxide composite (PBGO) can be applied to SIC as a battery-type cathode. PBGO is synthesized by a single-step decomposition method and has a morphology in which graphene oxide covered Prussian blue, which has a uniform cubic structure. PBGO exhibit a high capacity of 165 mAh g^{-1} at 20 mA g^{-1}, as well as 68 mAh g^{-1} at a high current density of 4 A g^{-1}. The SIC is fabricated using PBGO as the cathode materials and activated carbon (AC) as a capacitor-type anode, and it exhibit a high specific energy density of 65.3 Wh kg^{-1} and a superior capacity retention of 78.8% after 10,000 cycles. The use of battery-type cathodes presents a promising strategy for developing SIC with high energy and long lifespan.

1. Introduction

With increasing interest in electric vehicles and energy storage systems, extensive research has been conducted on energy storage materials with high storage capacity and high power [1–3]. Lithium-based batteries have attracted considerable attention for decades [4–6]. However, the continued rise of lithium prices, uneven distribution of resources and the limited amount of lithium are major obstacles in the development of energy storage materials using lithium. Sodium, which has similar physicochemical properties, is considered to be a sustainable candidate for replacing lithium due to its abundant resources on Earth and relatively low price [7–9]. However, similar to lithium-ion batteries (LIBs), sodium-ion batteries (SIBs) have a low power density and it is difficult to meet the demands of commercial energy storage system. To solve this problem, sodium-ion capacitors (SICs) are proposed that combines the high power of a capacitor-type material and the high energy of a battery-type material [10–13].

A typical configuration of the hybrid system is to assemble into a single cell, a battery-type material having plateaus during charging and discharging and a capacitor-type material storing energy through adsorption and desorption of surfaces [14]. This combination allows for high energy and high power. Lee's group [15] achieved excellent performance by constructing a hybrid system combining a battery-type $NaTi_2(PO_4)_3$ and a capacitor-type graphene nanosheet. The Zhou group and Wasinski group reported a combination of a battery-type cathode, P2-$Na_{0.67}Co_{0.5}Mn_{0.5}O_2$ and $Na_{0.4}MnO_2$, and a capacitor-type anode [16,17]. These findings not only show the promise of hybrid systems but also that sodium pre-intercalated battery-type materials have desirable properties to be applicable to hybrid systems.

Among the various materials in which sodium is pre-intercalated, Prussian blue and its analogue have been continuously studied for the following reasons [18–20]. Prussian blue can be easily synthesized using a single precursor and has an open framework structure, hence it is possible to insert and extract sodium ions smoothly. Additionally, it has a theoretical capacity of approximately 171 mAh g^{-1} through two redox reactions. However, restricted utilization of sodium ions by water molecules occupying $[Fe(CN)_6]$ vacancies and low stability of PBs are the main factors that limit its use. In order to solve this problem, researchers have reduced the $[Fe(CN)_6]$ vacancies by introducing graphene oxide, and as a result, capacity reduction is prevented and the cycle stability is improved [21].

Herein, we report the application of PB and graphene oxide composites (PBGO) to upside-down SICs, comprising a battery-type cathode and capacitor-type anode. PB was synthesized through decomposition of a single precursor under acidic conditions. PBGO was prepared by introducing graphene oxide during the PB synthesis

* Corresponding authors.
E-mail addresses: leeys@jnu.ac.kr (Y.-S. Lee), ypark@jnu.ac.kr (Y.I. Park).

https://doi.org/10.1016/j.jallcom.2021.162952
0925-8388/

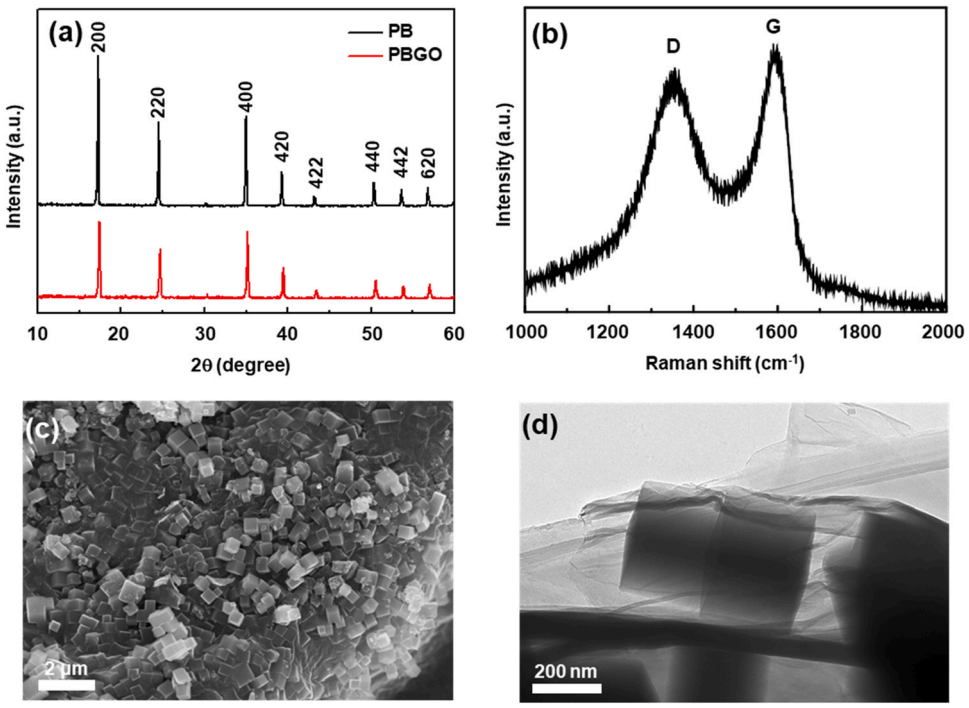

Fig. 1. (a) XRD patterns of PB and PBGO; (b) Raman spectrum of PBGO; (c) SEM image of PBGO; (d) TEM image of PBGO.

process. Through a graphene oxide sheet, the capacity contribution of the surface capacitive process was increased, resulting in a better rate performance at high current densities. Also, the application of PBGO to the SICs as a cathode was carried out and has been confirmed to have good cyclability and high power-energy densities compared to pure PB.

2. Experimental procedure

2.1. Synthesis of PB and PBGO

The PB was prepared through a previously reported method, which involved the decomposition of sodium ferrocyanide ($Na_4Fe(CN)_6$, Sigma Aldrich, 99%) [18]. We dissolved sodium ferrocyanide (4 mmol) in distilled water (100 mL), and then, hydrochloric acid (1 mL, Daejung, 37%) was added to the solution. After stirring at 60 ℃ for 4 h, the as-synthesized PB was washed several times with water and ethanol and dried overnight at 80 ℃ under vacuum. For the PBGO, 200 mg of graphene oxide (standard graphene) was added to the reaction solution while stirring at 60 ℃.

2.2. Characterization

The crystalline structures of the samples were analyzed by an X-ray diffractometer (XRD, Rigaku Rint 1000, Japan) with a Cu Kα radiation source. The morphologies of the samples were examined using scanning electron microscopy (SEM, Hitachi SU-70, Japan) and transmission electron microscopy (TEM, TECNAI G2 F20, USA). The content of graphene oxide in PBGO was calculated using thermogravimetric analysis (TGA, DTG-60H, Japan) and differential thermal analysis (DTA, DTG-60H, Japan). Raman spectra of the samples were recorded using a LabRam HR800 UV Raman microscope (Horiba Jobin-Yvon, France). Fourier-transform infrared spectra (FT-IR) was measured using IR Prestige-21 spectrometer (Shimadzu, Japan). The specific surface area and pore size distribution were calculated by Brunauer–Emmett–Teller (BET) analysis (ASAP2020, Micromeritics, USA). The chemical states of PB and PBGO were determined by X-ray photoelectron spectroscopy (XPS) measurements (K-ALPHA+, Thermo Scientific, USA).

2.3. Electrochemical measurement

The half-cell performance of the PB and PBGO was performed on a 2032-type coin cell with a Na metal film as the anode. The electrode material was prepared by mixing active materials, Ketjen black, and teflonized acetylene black (TAB) in a weight ratio of 5:1:1. The mixture was pressed onto a stainless steel current collector and dried for 4 h in a vacuum oven at 160 ℃. The electrolyte was prepared by mixing 1 M $NaClO_4$, propylene carbonate (PC), and 2 wt% fluoroethylene carbonate (FEC) additive. The coin cell was then assembled in an argon-filled glove box. The working electrode and the metallic sodium anode were separated by a porous separator (glass fiber from Whatman). A Won-A-Tech battery tester (WBCS 3000, Korea) was used for galvanostatic charge-discharge tests in the voltage range of 2.0–4.2 V vs. Na/Na^+. Cyclic voltammetry (CV) and electrochemical impedance spectroscopy (EIS) measurements were performed using Bio-Logic electrochemical workstation (SP-150, France) at various scan rates within the potential range of 2.0–4.2 V vs. Na/Na^+. The electrical conductivity and diffusion coefficient were calculated by fitting the EIS results with ZMAN program. The diffusion coefficients (D_{Na}) were calculated by the following equations:

$$D_{Na} = \frac{R^2T^2}{2A^2n^4F^4C_{Na}{}^2\sigma^2} \quad (1)$$

$$Z' = R_{ct} + R_s + \sigma\omega^{-\frac{1}{2}} \quad (2)$$

In Eq. (1), R is the gas constant (J mol^{-1} K^{-1}), T is the absolute temperature (K), A is the electrode area (cm^2), n is the number of electron transfer, F is the Faraday constant (96,485 C mol^{-1}), C_{Na} is the concentration of Na^+ (mol cm^{-3}), and σ is Warburg factor. The σ value can be obtained from Eq. (2). The linear relationship was observed between Z′ and $\omega^{-1/2}$ in the low-frequency region, and the slope of this linear plot is σ value.

The capacitor system was also prepared in a manner similar to the half-cell system. Activated carbon (AC) was used as the anode

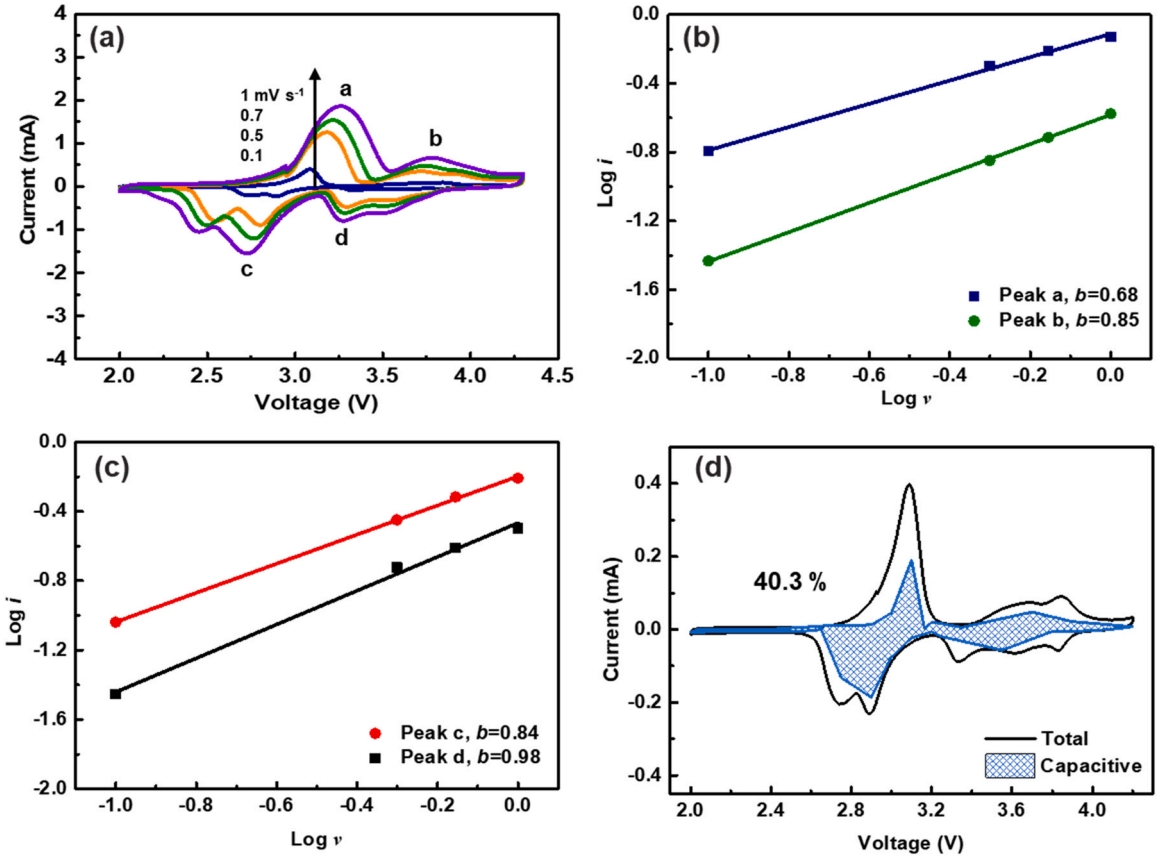

Fig. 2. (a) CV curves of PBGO at different sweep rates from 0.1 to 1.0 mV s^{-1}; The log (specific *i*) versus log(*v*) plot and *b* values of the (b) anodic peaks and (c) cathodic peaks; (d) CV curve of PBGO with separation of the contribution to surface capacitive storage (shaded regions) at 0.1 mV s^{-1}.

material (Fig. S1), and a mixture of 1 M $NaClO_4$ and ethylene carbonate (EC) and dimethyl carbonate (DMC) (EC:DMC=1:1) was used as the electrolyte. Measurements for the galvanostatic charge-discharge profile and CV over the range of 0.01–3.5 V were also carried out using the same equipment. The energy density (Whkg^{-1}) and power density (Wkg^{-1}) of the SIC was calculated using the following equations:

$$\text{Energy density (E, Wh kg}^{-1}) = \int_{t_1}^{t_2} IVdt \quad (3)$$

$$\text{Power density(P, W kg}^{-1}) = \frac{E}{t} \quad (4)$$

where t_1 (s) and t_2 (s) are the start and end times of cell discharge, I (A g^{-1}) is the current density, V (V) is the working voltage, and t (s) is the discharge time.

3. Results and discussion

3.1. Characterization of PB and PBGO

The PB was synthesized by the decomposition of $Na_4Fe(CN)_6$ at 60 ℃ under acidic condition. During the synthesis, $[Fe(CN)_6]^{4-}$ was decomposed into Fe^{2+}, and some of this Fe^{2+} was subsequently oxidized to Fe^{3+}. The resulting Fe^{3+} ions reacted with $[Fe(CN)_6]^{4-}$ to form PB seeds. Thereafter, the PB seeds grew gradually over the reaction time. The PBGO was synthesized by adding graphene oxide during PB formation. The chemical composition of PB and PBGO was confirmed by FT-IR and XPS analysis (Fig. S2). The peak at 2083 cm^{-1} of the FT-IR spectrum corresponds to the stretching vibration of C≡N, and the peaks in the XPS spectrum was assigned as Fe^{3+} ($2p_{1/2}$ and $2p_{3/2}$) and Fe^{2+} ($2p_{1/2}$ and $2p_{3/2}$). Both PB and PBGO showed similar FT-IR patterns, and the XPS peaks of PBGO shifted to a higher binding energy, suggesting that PBGO was formed by electrostatic interaction between PB and GO.

Fig. 1a shows the XRD patterns of PB and PBGO. The XRD peaks of PB and PBGO were indexed to ferric ferrocyanide (JCPDS No. 73–0687), indicating that both had a face-centered cubic (FCC) crystal structure (space group $Fm\bar{3}m$), which implies that the added graphene oxide did not affect the crystal structure of the PB. In the case of PBGO, the prominent graphite peaks (especially, 2θ = 26°, corresponding to the (002) plane of graphite) were not observed. This demonstrates that there is no aggregation of graphene oxide in the process of the reaction.

In addition, the presence of the graphene oxide in the PBGO is confirmed by Raman spectrum analysis. In the Raman spectrum, D band and G band peaks are observed between 1300 and 1600 cm^{-1}, which correspond to the disordered carbon and graphitic carbon, respectively (Fig. 1b). The I_D/I_G ratio is calculated to be 0.91, which means that the graphene oxide of the composite can improve the conductivity of the active material and improve the rate performance of the SIC [22]. The specific content of the graphene oxide in the synthesized PBGO was calculated as 17.6% using TGA and DTA (Fig. S3).

The morphology of each sample was characterized using SEM and TEM. The SEM images (Figs. 1c and S4) show that these samples have cubic shapes with various sizes ranging from 200 nm to 1 μm. The size difference among PB samples is prominent in pure PB samples than in PBGO. Compared with PB, PBGO has a uniform size (approximately 300 nm). This uniform size distribution was contributed by the graphene oxide layer. This layer limited the aggregation and the growth of PB seeds. Furthermore, The TEM image in Fig. 1d supports the fact that the PB samples are covered and

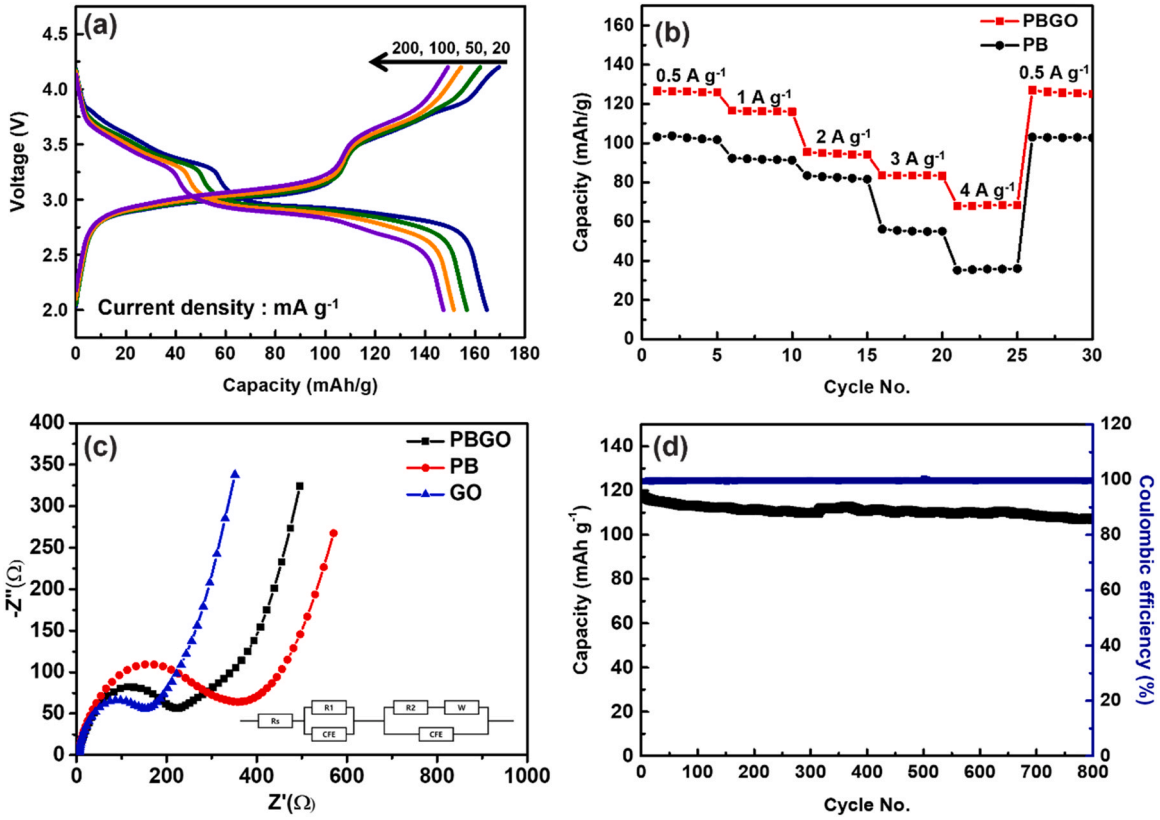

Fig. 3. (a) Galvanostatic charge-discharge voltage profiles of PBGO; (b) Rate performance of PB and PBGO at high current densities; (c) Nyquist plots of PB, PBGO, and GO; (d) Long cyclic performance of PBGO at 500 mA g^{-1}.

connected by a 3D graphene oxide network. The interaction of PB and graphene oxide network utilizes the high electrical conductivity of graphene oxide and facilitates electron transfer between PB samples, thereby contributing to higher electrochemical performance.

3.2. Half-cell performance

Half-cell test of PB and PBGO was performed on a coin cell with metallic sodium as a counter electrode. CV of the samples was measured in the voltage range of 2.0–4.2 V vs. Na/Na^+ at scan rates of 0.1, 0.5, 0.7 and 1 mV s^{-1} (Fig. 2a). Several pairs of peaks are identified at scan rate of 0.1 mV s^{-1}, with prominent peaks appearing in the voltage range of 2.8–3.2 V (vs. Na / Na^+). These may be explained by Fe^{2+}/Fe^{3+} redox activities and different intercalation sites for sodium ions. Several other peaks were considered to occur stepwise in the extraction and insertion of sodium ions during charging and discharging.

To further analyze the charge and discharge mechanism, we examined the kinetics of the PBGO composite. In Fig. 2a, two anodic peaks (a and b) and two cathodic peaks (c and d) are observed. The relation between current (i) and scanning rate (v) follows the power law [23]. In $i = av^b$, the value of b is representative of the charge and discharge mechanism. If the value of b is closer to 0.5, the diffusion insertion process is more dominant, and if it is closer to 1.0, the surface capacitive process dominates. As shown in Figs. 2b and c, the values of b at the anodic and cathodic peaks are 0.68, 0.85, 0.84, and 0.98, respectively, indicating that the charging and discharging process is a combination of diffusion insertion and surface capacitive processes. Except for the peak a, other peaks are close to 1.0. This indicates that surface capacitive reactions, with relatively faster kinetics, are more dominant than the diffusion insertion process. In contrast, the peak a originates from the diffusion insertion process. Moreover, to quantify the contributions from diffusion insertion and the surface capacitive process, we use equation (5) [24,25]:

$$i = k_1 v + k_2 v^{0.5} \quad (5)$$

where v is the scanning rate (mV s^{-1}), i is the specific current (A g^{-1}) at a certain potential, and k_1 and k_2 are constants. In this equation, $k_1 v$ and $k_2 v^{0.5}$ are the contributions of the surface capacitive and diffusion insertion processes at a certain potential, respectively. By dividing each term of equation (5) by $v^{0.5}$ and plotting with $v^{0.5}$ versus $i\ v^{-0.5}$, the values of k_1 and k_2 can be obtained (Fig. S5). Following this analysis, similar to the result of the power law, the surface capacitive reaction is dominant. The contribution of the surface capacitive process increases as the scanning rate increases (Fig. S6). Particularly, the peak a increases from approximately 55–77%. Consequently, compared with the pure PB sample, the surface capacitive contribution, which is approximately 26.7% in PB, is shown to increase to 40.3% in PBGO at the scanning rate of 0.1 mV s^{-1} (Fig. 2d, Fig. S7). This increase in the contribution of fast kinetics is due to the effect of the graphene oxide network, which results in better rate performance than pure PB in the half and full cell.

Fig. 3a shows the galvanostatic charge-discharge voltage profile of PBGO at various current densities from 20 mA g^{-1} to 200 mA g^{-1}. The discharge capacities at each current density are 165, 157, 151 and 147 mAh g^{-1}. The multi plateaus during charge and discharge correspond to the redox reaction of iron-ions, indicating that the insertion and extraction of Na^+ ions occur step by step. Concretely, plateaus with a voltage ranging from 2.8 V to 3.2 V correspond to the redox reaction of the Fe2 site, and the plateaus in the high voltage range represent the redox process of the Fe1 site [21,26]. The rate performance is verified to compare the electrochemical performance of pure PB and PBGO at high current densities (Fig. 3b and Fig. S8b).

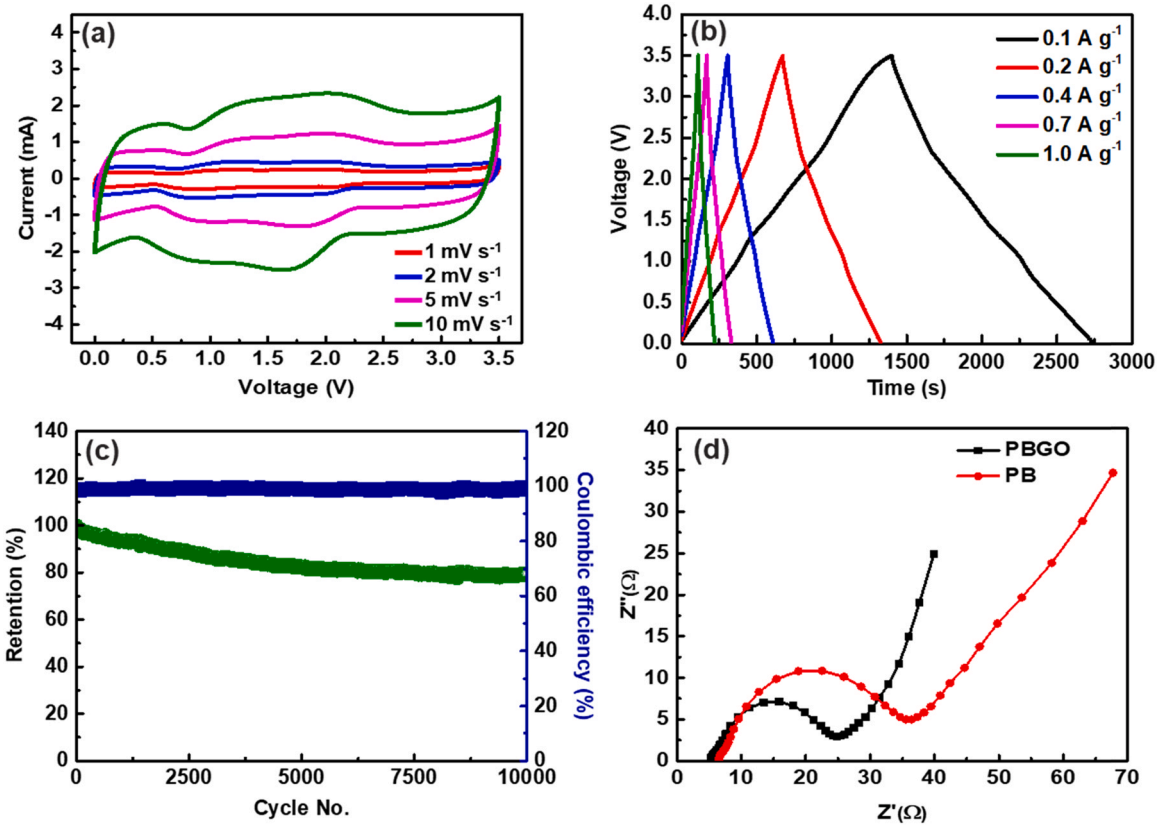

Fig. 4. (a) CV curves of PBGO//AC at various sweep rates; (b) Charge-discharge curves of PBGO at various current densities; (c) Cyclic performance of PBGO at 1 A g^{-1}; (d) Nyquist plots of the sodium-ion capacitors cells with PB and PBGO.

At a current density of 4 A g^{-1}, only about 36 mAh g^{-1} of capacity remained in pure PB, whereas for PBGO, approximately 68 mAh g^{-1} of capacity remain. Fig. 3c shows the Nyquist plots of PBGO, PB, and GO. The semicircle at high frequency can be ascribed to the charge transfer resistance (R_{ct}). The R_{ct} values of PB, PBGO and GO were calculated to be 330 Ω, 247 Ω and 179 Ω, respectively, indicating that the electrical conductivity of PBGO was improved compared to PB. The diffusion coefficients of sodium ions in PB and PBGO were calculated to be 1.91×10^{-13} cm^2 s^{-1} and 1.05×10^{-13} cm^2 s^{-1}, respectively (Eq. 1 and Fig. S9). The GO on the PBGO surface lowered the diffusivity of sodium ions into the PB, but the increase in electrical conductivity by GO seems to improve the rate performance. Furthermore, PBGO exhibits high stability of approximately 91.3% retention after 800 cycles at a current density of 0.5 A g^{-1} (Fig. 3d). These half-cell test results are summarized as follows. By introducing graphene oxide, there is increased capacity contribution of the surface capacitive process, with relatively fast kinetics. This contribution improvement has the effect of alleviating the decrease in capacity as the high current density.

3.3. Sodium-ion hybrid energy storage

The performance of the SICs have been evaluated in 1:1 mass ratio and 0.01–3.5 V range using the combination of PBGO with AC. The CV curves shown in Fig. 4a show asymmetrical rather than perfect rectangular curves and have partially broad redox peaks. This shape indicates that the reaction mechanism of the hybrid system includes non-Faradaic adsorption/desorption onto the surface of PBGO and Faradaic intercalation/extraction of sodium ions into PBGO, matching with redox peaks. According to the CV curves, the galvanostatic charge-discharge curves of SIC also exhibit an asymmetric structure with the plateau related with rather than a completely triangular shape (Fig. 4b). The cyclic performance is evaluated at the current density of 1 A g^{-1} (Fig. 4c). After testing for 10,000 cycles, PBGO maintains retention of approximately 78.8% and a Coulombic efficiency of approximately 99.0%. This stable performance results from smooth Na^+ ion insertion and extraction by the unique open framework structure, which is a characteristic of PB (Fig. S10). Graphene oxide also mitigates the volume change of PB generated during the charging and discharging process and smoothens electron transfer. SEM image and ex-situ XPS spectrum of PBGO after 1000 cycles indicate that PBGO maintains its structure well during repeated charging and discharging (Fig. S11).

The EIS data in the form of Nyquist plots demonstrate the superior performance of PBGO compared to pure PB and graphene oxide (Fig. 4d). A semicircle in the high-frequency region indicates the charge transfer reaction between the electrode and the electrolyte. An inclined line in the low-frequency region explains the effect of insertion and extraction of Na^+ ions. The high-frequency region indicates that PBGO has lower charge transfer resistance than PB. This decrease in resistance might be attributed to the graphene oxide layer of PBGO because it provides a more efficient means to transfer electrons between PB active sites.

The Ragone plots show the energy and power density calculated with the total mass of both electrodes (Fig. 5a). The highest energy density is 65.3 Wh kg^{-1}, and the energy density has high retention when the power density of these SICs is increased by 3500 W kg^{-1}. These results indicate that the PBGO//AC system has more energy and power density than lithium-ion capacitors (LICs) assembled with AC such as $LiCoO_2$//AC [27], $LiCoPO_4F$//AC [28], $Li_3V_2(PO_4)_3$//AC [29], $Li_4Ti_5O_{12}$//AC [30], and Li_2MnSiO_4//AC [31]. Additionally, compared to the previously reported SICs based on $NaMnO_2$ [17], $Na_{0.67}Co_{0.5}Mn_{0.5}O_2$ [16], V_2O_5/CNT nanowire [32], $Na_2Ti_3O_7$ [33], and

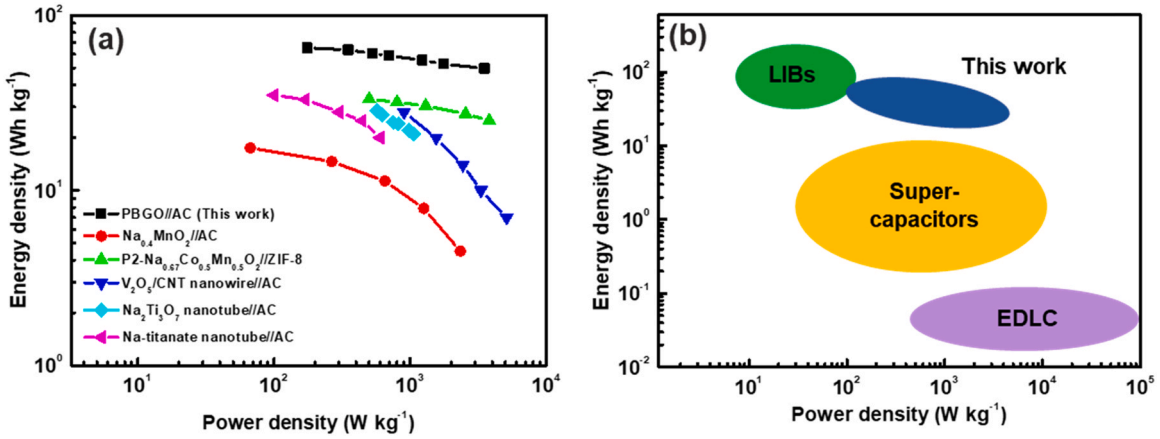

Fig. 5. (a) Ragone plot for the PBGO//AC SIC based on the total mass of both electrodes compared with data in the literature; (b) Device-based performance compared with other high-power devices.

Na-titanate nanotubes [34], this novel SIC system is shown to be superior.

4. Conclusion

In summary, we prepared PBGO with a facile decomposition method and designed an upside-down SIC full-cell consisting of PBGO (battery-type cathode) and AC (capacitor-type anode). The introduction of graphene oxide improves the contribution of the surface capacitive process, which results in good rate performance at high current densities. Moreover, the combination of the open framework structure of PB with the graphene oxide network provides an efficient pathway of sodium-ion and electron transfer, resulting in a high cyclic stability of 78.8% after 10,000 cycles as in SICs. Consequently, this study achieves superior performance compared with previous upside-down SICs and can be a candidate of energy storage systems with high energy density and power density.

CRediT authorship contribution statement

Song Yeul Lee: Conceptualization, Methodology, Validation, Formal analysis, Investigation, Writing – original draft, Writing – review & editing. **Joo-Yeon Park:** Investigation. **Hyun-Jae Kim:** Investigation. **Yun-Sung Lee:** Conceptualization, Supervision, Project administration, Funding acquisition. **Yong Il Park:** Conceptualization, Methodology, Validation, Writing – original draft, Writing – review & editing, Supervision, Project administration, Funding acquisition.

Declaration of Competing Interest

The authors declare that they have no known competing financial interests or personal relationships that could have appeared to influence the work reported in this paper.

Acknowledgements

This work was supported by the National Research Foundation of Korea (NRF) grant funded by the Korea government (Ministry of Science, ICT & Future Planning) (No. 2019R1A4A2001527).

Appendix A. Supporting information

Supplementary data associated with this article can be found in the online version at doi:10.1016/j.jallcom.2021.162952.

References

[1] Y. Gogotsi, P. Simon, True performance metrics in electrochemical energy storage, Science 334 (2011) 917–918, https://doi.org/10.1126/science.1213003
[2] M. Winter, B. Barnett, K. Xu, Before Li ion batteries, Chem. Rev. 118 (2018) 11433–11456, https://doi.org/10.1021/acs.chemrev.8b00422
[3] H. Zhang, X. Yu, P.V. Braun, Three-dimensional bicontinuous ultrafast-charge and -discharge bulk battery electrodes, Nat. Nanotechnol. 6 (2011) 277–281, https://doi.org/10.1038/nnano.2011.38
[4] A.K. Padhi, K.S. Nanjundaswamy, J.B. Goodenough, Phospho-olivines as positive-electrode materials for rechargeable lithium batteries, J. Electrochem. Soc. 144 (1997) 1188–1194, https://doi.org/10.1149/1.1837571
[5] C.K. Chan, H. Peng, G. Liu, K. McIlwrath, X.F. Zhang, R.A. Huggins, Y. Cui, High-performance lithium battery anodes using silicon nanowires, Nat. Nanotechnol. 3 (2008) 31–35, https://doi.org/10.1038/nnano.2007.411
[6] P. Poizot, S. Laruelle, S. Grugeon, L. Dupont, J.M. Tarascon, Nano-sized transition-metal oxides as negative-electrode materials for lithium-ion batteries, Nature 407 (2000) 496–499, https://doi.org/10.1038/35035045
[7] M.D. Slater, D. Kim, E. Lee, C.S. Johnson, Sodium-ion batteries, Adv. Funct. Mater. 23 (2013) 947–958, https://doi.org/10.1002/adfm.201200691
[8] J.-Y. Hwang, S.-T. Myung, Y.-K. Sun, Sodium-ion batteries: present and future, Chem. Soc. Rev. 46 (2017) 3529–3614, https://doi.org/10.1039/C6CS00776G
[9] J. Yang, J. Li, T. Wang, P.H.L. Notten, H. Ma, Z. Liu, C. Wang, G. Wang, Novel hybrid of amorphous Sb/N-doped layered carbon for high-performance sodium-ion batteries, Chem. Eng. J. 407 (2021) 127169, https://doi.org/10.1016/j.cej.2020.127169
[10] Z. Sun, K. Zhu, P. Liu, Y. Si, H. Li, L. Jiao, Rapid kinetics of Na-ion storage in bimetallic sulfide composite, Energy Storage Mater. 41 (2021) 32–40, https://doi.org/10.1016/j.ensm.2021.05.041
[11] J. Tan, W. Zhu, Q. Gui, Y. Li, J. Liu, Weak ionization induced interfacial deposition and transformation towards fast-charging $NaTi_2(PO_4)_3$ nanowire bundles for advanced aqueous sodium-ion capacitors, Adv. Funct. Mater. 31 (2021) 2101027, https://doi.org/10.1002/adfm.202101027
[12] X. Deng, K. Zou, R. Momen, P. Cai, J. Chen, H. Hou, G. Zou, X. Ji, High content anion (S/Se/P) doping assisted by defect engineering with fast charge transfer kinetics for high-performance sodium ion capacitors, Sci. Bull. 66 (2021) 1858–1868, https://doi.org/10.1016/j.scib.2021.04.042
[13] X. Deng, K. Zou, P. Cai, B. Wang, H. Hou, G. Zou, X. Ji, Advanced battery-type anode materials for high-performance sodium-ion capacitors, Small Methods 4 (2020) 2000401, https://doi.org/10.1002/smtd.202000401
[14] A.M. Glushenkov, A.V. Ellis, Cell configurations and electrode materials for nonaqueous sodium-ion capacitors: the current state of the field, Adv. Sustain. Syst. 2 (2018) 1800006, https://doi.org/10.1002/adsu.201800006
[15] R. Thangavel, B. Moorthy, D.K. Kim, Y.-S. Lee, Pushing the energy output and cyclability of sodium hybrid capacitors at high power to new limits, Adv. Energy Mater. 7 (2017) 1602654, https://doi.org/10.1002/aenm.201602654
[16] H. Gu, L. Kong, H. Cui, X. Zhou, Z. Xie, Z. Zhou, Fabricating high-performance sodium ion capacitors with P2-$Na_{0.67}Co_{0.5}Mn_{0.5}O_2$ and MOF-derived carbon, J. Energy Chem. 28 (2019) 79–84, https://doi.org/10.1016/j.jechem.2018.01.012
[17] K. Wasiński, P. Półrolniczak, M. Walkowiak, Proof-of-concept study of a new type sodium-ion hybrid electrochemical capacitor with organic electrolyte, Electrochim. Acta 259 (2018) 850–854, https://doi.org/10.1016/j.electacta.2017.11.036
[18] Y. You, X.-L. Wu, Y.-X. Yin, Y.-G. Guo, High-quality Prussian blue crystals as superior cathode materials for room-temperature sodium-ion batteries, Energy Environ. Sci. 7 (2014) 1643–1647, https://doi.org/10.1039/C3EE44004D
[19] J. Peng, J. Wang, H. Yi, W. Hu, Y. Yu, J. Yin, Y. Shen, Y. Liu, J. Luo, Y. Xu, P. Wei, Y. Li, Y. Jin, Y. Ding, L. Miao, J. Jiang, J. Han, Y. Huang, A dual-insertion type sodium-ion full cell based on high-quality ternary-metal Prussian blue analogs, Adv. Energy Mater. 8 (2018) 1702856, https://doi.org/10.1002/aenm.201702856

[20] Y. Lu, L. Wang, J. Cheng, J.B. Goodenough, Prussian blue: a new framework of electrode materials for sodium batteries, Chem. Commun. 48 (2012) 6544–6546, https://doi.org/10.1039/C2CC31777J
[21] D. Yang, J. Xu, X.-Z. Liao, H. Wang, Y.-S. He, Z.-F. Ma, Prussian blue without coordinated water as a superior cathode for sodium-ion batteries, Chem. Commun. 51 (2015) 8181–8184, https://doi.org/10.1039/C5CC01180A
[22] C. Wu, P. Kopold, Y.-L. Ding, P.A. van Aken, J. Maier, Y. Yu, Synthesizing porous $NaTi_2(PO_4)_3$ nanoparticles embedded in 3D graphene networks for high-rate and long cycle-life sodium electrodes, ACS Nano 9 (2015) 6610–6618, https://doi.org/10.1021/acsnano.5b02787
[23] D. Su, K. Kretschmer, G. Wang, Improved electrochemical performance of Na-ion batteries in ether-based electrolytes: a case study of ZnS nanospheres, Adv. Energy Mater. 6 (2016) 1501785, https://doi.org/10.1002/aenm.201501785
[24] J. Wang, J. Polleux, J. Lim, B. Dunn, Pseudocapacitive contributions to electrochemical energy storage in TiO_2 (anatase) nanoparticles, J. Phys. Chem. C 111 (2007) 14925–14931, https://doi.org/10.1021/jp074464w
[25] H.B. Wu, J.S. Chen, H.H. Hng, X. Wen Lou, Nanostructured metal oxide-based materials as advanced anodes for lithium-ion batteries, Nanoscale 4 (2012) 2526–2542, https://doi.org/10.1039/C2NR11966H
[26] Y. Jiang, S. Yu, B. Wang, Y. Li, W. Sun, Y. Lu, M. Yan, B. Song, S. Dou, Prussian blue@C composite as an ultrahigh-rate and long-life sodium-ion battery cathode, Adv. Funct. Mater. 26 (2016) 5315–5321, https://doi.org/10.1002/adfm.201600747
[27] S.L. Zhang, L.H. Ma, X.G. Li, Y.H. Song, W. Li, Research on lithium ion battery material $LiCoO_2$ for hybrid supercapacitor, Adv. Mat. Res. 287–290 (2011) 1565–1568, https://doi.org/10.4028/www.scientific.net/AMR.287-290.1565
[28] K. Karthikeyan, S. Amaresh, K.J. Kim, S.H. Kim, K.Y. Chung, B.W. Cho, Y.S. Lee, A high performance hybrid capacitor with Li_2CoPO_4F cathode and activated carbon anode, Nanoscale 5 (2013) 5958–5964, https://doi.org/10.1039/C3NR00760J
[29] R. Satish, V. Aravindan, W.C. Ling, S. Madhavi, Carbon-coated $Li_3V_2(PO_4)_3$ as insertion type electrode for lithium-ion hybrid electrochemical capacitors: an evaluation of anode and cathodic performance, J. Power Sources 281 (2015) 310–317, https://doi.org/10.1016/j.jpowsour.2015.01.190
[30] I. Plitz, A. DuPasquier, F. Badway, J. Gural, N. Pereira, A. Gmitter, G.G. Amatucci, The design of alternative nonaqueous high power chemistries, Appl. Phys. A 82 (2006) 615–626, https://doi.org/10.1007/s00339-005-3420-0
[31] K. Karthikeyan, V. Aravindan, S.B. Lee, I.C. Jang, H.H. Lim, G.J. Park, M. Yoshio, Y.S. Lee, Electrochemical performance of carbon-coated lithium manganese silicate for asymmetric hybrid supercapacitors, J. Power Sources 195 (2010) 3761–3764, https://doi.org/10.1016/j.jpowsour.2009.11.138
[32] Z. Chen, V. Augustyn, X. Jia, Q. Xiao, B. Dunn, Y. Lu, High-performance sodium-ion pseudocapacitors based on hierarchically porous nanowire composites, ACS Nano 6 (2012) 4319–4327, https://doi.org/10.1021/nn300920e
[33] L. Zhao, L. Qi, H. Wang, Sodium titanate nanotube/graphite, an electric energy storage device using Na^+-based organic electrolytes, J. Power Sources 242 (2013) 597–603, https://doi.org/10.1016/j.jpowsour.2013.05.132
[34] J. Yin, L. Qi, H. Wang, Sodium titanate nanotubes as negative electrode materials for sodium-ion capacitors, ACS Appl. Mater. Interfaces 4 (2012) 2762–2768, https://doi.org/10.1021/am300385r